Langmuir

Article

pubs.acs.org/Langmuir

Isolation and Characterization of Monodisperse Core−Shell Nanoparticle Fractions

Antoni Sánchez-Ferrer,[†] Randy P. Carney,[‡] Francesco Stellacci,[‡] Raffaele Mezzenga,[†] and Lucio Isa*[,§]

[†]Laboratory of Food and Soft Matter, Department of Health Sciences and Technology, ETH Zurich, Schmelzbergstrasse 9, CH-8092 Zurich, Switzerland

[‡]Institute of Materials, Ecole Polytechnique Fédérale de Lausanne, CH-1015 Lausanne, Switzerland

[§]Laboratory for Interface, Soft matter and Assembly, Department of Materials, ETH Zurich, Vladimir-Prelog-Weg 5, CH-8093 Zurich, Switzerland

Supporting Information

ABSTRACT: Monodispersity is a key property to control the self-assembly of colloidal particles, and is typically reached after fine-tuning of the synthesis conditions. Monodisperse particle fractions can also be separated from polydisperse suspensions via ultracentrifugation. This paper demonstrates the capability of isolating and characterizing suspensions of core−shell iron oxide-polymer nanoparticles with extremely low polydispersity ($p < 0.01$) and, thus, of complementing nanoparticle synthetic approaches in the pursuit of highly monodisperse materials.

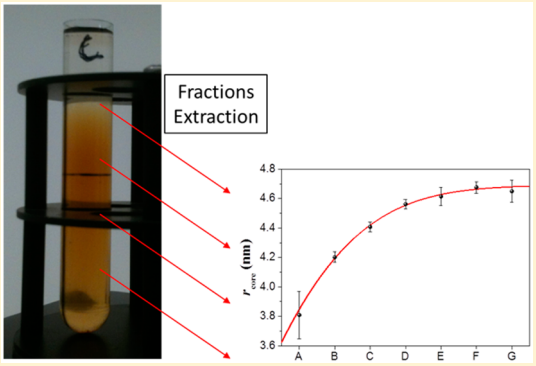

INTRODUCTION

Monodispersity is a crucial property in determining the microstructure and properties of colloidal materials.[1] Extensive structural studies have, for instance, demonstrated that ensembles of spherical particles fail to crystallize for polydispersities larger than 10%, and that simply adding a small percentage of slightly bigger or smaller particles slows down considerably the kinetics of crystallization.[2] High monodispersity is also necessary for the formation of complex nanoparticle (NP) suprastructures.[3] Numerous high-end applications can take advantage of monodisperse colloids, including batteries,[4] nanoparticle patterns,[5] plasmonic biosensors,[6] and nanoparticle transport through cell membranes.[7]

Nature can often produce monodisperse objects with specific functionality, including viruses (e.g., tobacco mosaic virus), peptides, and proteins. Most typically, monodispersity of man-made nanoscale objects is sought and achieved during nanoparticle synthesis, which often requires thorough and sensitive control of the reaction conditions to reach narrow size distributions. In some cases, monodisperse systems can only be achieved for certain size windows and sequences of growth steps may be required to bridge over different length scales.[8] Furthermore, in particle growth and nucleation processes, there are physical limitations for monodispersity, linked to the kinetics and thermodynamics of the reactions.[9]

A way to overcome these limitations and improve the outcome of synthetic processes is to separate monodisperse particle fractions after synthesis. Many strategies have been developed to perform this task, and include electrophoretic separation[10] and microfluidics.[11] One of the classical approaches employs centrifugation (or ultracentrifugation),[12] and it is commonly used to separate proteins in biology or isotopes in nuclear technology. The technique has seen a recent revival in particle technology,[13,14] partly due to improvements in data analysis, and it has been successfully applied to separate a large range of systems, including multivalent patchy particles in the micrometer range,[15,16] monodisperse silicon nanocrystals,[17,18] semiconductor quantum dots,[19] and metal NPs coated by different molecular capping agents.[20] Additional applications entailed the isolation of highly monodisperse graphene sheets[21] and the separation of carbon nanotubes by their length[22] and diameter,[23] respectively. So far ultracentrifugation has not been demonstrated for more complex core−polymer shell NPs, where both the uniformity of the shell and of the core sizes affect the separation. In this paper, we demonstrate that ultracentrifugation via rate zonal separation can be successfully applied to produce fractions of iron oxide nanoparticles stabilized by dendritic poly(ethylene glycol) (PEG) shells with extraordinarily small polydispersity values. We define polydispersity as $p = \sigma \cdot r_{core}^{-1}$, following the standard definition for small-angle scattering characterization of particulate systems,[24] where σ is the standard deviation of the size

Received: May 17, 2015
Revised: September 22, 2015
Published: September 25, 2015

DOI: 10.1021/acs.langmuir.5b01811
Langmuir 2015, 31, 11179−11185

distribution and r_{core} the average radius. Suspensions of particles with core radii continuously varying between 3.8 and 4.6 nm could be consistently achieved, with values of p down to the order of 10^{-4}. In order to characterize core size and shell thickness of all the NP fractions thoroughly, we carried out small-angle X-ray scattering (SAXS) experiments, offering significantly improved statistical analysis compared to electron microscopy characterization, as detailed later. Specifically, a spherical core−shell model together with a power-law model were used to fit the scattering signal coming from the core−shell NPs form factor and in order to include the effects of thermal fluctuations of the polymer shell, respectively. Our results indicate the capability of both isolating and characterizing polymer-stabilized NP fractions with unprecedented degrees of monodispersity, paving the way for future studies and applications where extremely small degrees of monodispersity are a key, for example, for optical applications or encapsulation.

EXPERIMENTAL SECTION

SAXS Measurements. The SAXS experiments were performed using a Rigaku MicroMax-002$^+$ microfocused beam (40 W, 45 kV, 0.88 mA). Cu Kα radiation ($\lambda_{CuK\alpha}$ = 1.5418 Å) was collimated by three pinhole collimators (0.4, 0.3, and 0.8 mm). The scattered X-ray intensity was detected by a two-dimensional Triton-200 gas-filled X-ray detector (20 cm diameter, 200 μm spatial resolution) covering a momentum transfer range of 0.1 nm^{-1} < q < 2 nm^{-1}, where $q = 4\pi\sin\theta/\lambda_{CuK\alpha}$, and 2θ is the scattering angle. The scattering intensity profiles were analyzed using the software SANS & USANS Analysis with IGOR Pro.[25]

In order to get information about the size and distribution of the core−shell spherical nanoparticles, small-angle X-ray scattering (SAXS) experiments were performed on aqueous dispersions of freeze-dried NPs at four different concentrations (0.24, 0.11, 0.059, and 0.024 wt %) for the pristine dispersion after synthesis and on the seven fractions after ultracentrifugation separation. Samples were frozen by plunging in liquid nitrogen and then freeze-dried in a Christ Alpha 1−2 LD Plus freeze drier (Germany) at a pressure of 0.086 mbar and a temperature of −52 °C. First, all scattering data were dark-current and transmission corrected and the corrected capillary signal was subtracted. Second, the concentration factor and the solvent subtraction were conducted for all samples in order to verify that all scattering profiles fell on the same master curve, indicating that the concentrations were sufficiently diluted to leave only the form factor $P(q) \sim I(q)/c$ visible in the curves, with the structure factor $S(q)$ independent from concentration and $S(q) = 1$ (Supporting Information Figure SI-1). Then, the form factors $P(q)$ were calculated from the corresponding scattering patterns of the highest concentration by applying a spherical polydisperse core−shell particle model keeping the thickness (t_{shell}) of the dendritic PEG shell constant and estimating the radius of the core (r_{core}) and its polydispersity ($p = \sigma \cdot r_{core}^{-1}$). The scattering length densities used for the magnetite core and the solvent (water) were ρ_{core} = 4.2271 × 10^{-3} nm^{-2} and ρ_{water} = 9.5096 × 10^{-4} nm^{-2}, respectively. For the polymer shell, a constant value of ρ_{shell} = 9.8450 × 10^{-4} nm^{-2} was found and kept constant for all the samples due to the nature of the monodisperse dendritic PEG polymer. Finally, a power-law model was included in order to adjust the intensity of the scattering signal at low q values coming from the fluctuations of the polymer shell, where the intensity profile was $I(q) = k_1 \cdot q^{-n} + k_2 \cdot P(q) + bkg$, where bkg was the background scattered intensity.

The form factor $P(q)$ for the polydisperse core−shell spheres can be constructed from the form factor of a monodisperse core−shell sphere[26,27]

$$P_{mono}(q) \propto \frac{1}{V_{NP}}\left[\frac{3V_{core}(\rho_{core}-\rho_{shell})(\sin(qr_{core})-qr_{core}\cos(qr_{core}))}{(qr_{core})^3} + \frac{3V_{NP}(\rho_{shell}-\rho_{water})(\sin(qr_{NP})-qr_{NP}\cos(qr_{NP}))}{(qr_{NP})^3}\right]^2$$

where $r_{NP} = r_{core} + t_{shell}$, $V_{core} = (4/3)\pi r_{core}^3$ and $V_{NP} = (4/3)\pi r_{NP}^3$.

The form factor for a polydisperse core−shell sphere is then defined as

$$P(q) = \int_0^\infty f(r_{core}) r_{core}^6 P_{mono}(q) \mathrm{d}r_{core}$$

where

$$f(r_{core}) = (z+1)^{z+1}\left(\frac{r_{core}}{\langle r_{core}\rangle}\right)^z \frac{e^{-(z+1)r_{core}/\langle r_{core}\rangle}}{\langle r_{core}\rangle \Gamma(z+1)}$$

is the Schulz distribution[28,29] with

$$\langle r_{core}\rangle^3 = \langle r_{core}\rangle^3 \frac{(z+3)(z+2)}{(z+1)^2}$$

$$\langle V_{core}\rangle = \frac{4}{3}\pi\langle r_{core}\rangle^3 \frac{(z+3)(z+2)}{(z+1)^2}$$

$$p = \frac{\sigma_{core}}{\langle r_{core}\rangle}$$

and

$$z = \frac{1}{p^2} - 1$$

where p is the polydispersity as defined in the main text, and z is the Schulz width parameter.

Ultracentrifugation. For nanoparticle fractionation, a Gradient Station (BioComp Instruments, Inc.) was utilized. Briefly, stock solutions of NPs were prepared in ultrapure water (Milli-Q) at a concentration of 10 mg·mL^{-1}. Then, 200 μL of the NP stock was loaded onto 12 mL of 20−50 wt % sucrose gradients in SW41 tubes (Beckman Coulter, Inc.) for rate zonal separation. NPs were centrifuged at 39 krpm for 2 h at 20 °C. The samples were manually fractionated via piston gradient fractionation in 3 mm wide slices, retaining every other fraction. Identical fractions were pooled across tubes and purified from sucrose by centrifugal filter dialysis (Amicon Ultra 15 Centrifugal Filter Units). We emphasize here that the colloidal stability of our iron oxide-PEG nanoparticles allowed removing sucrose residues via dialysis without any aggregation as a result of purification. We chose sucrose gradients for ease of operation and to be able to reach high resolution in the isolation of fractions in a narrow size range, but, strictly speaking, density gradients are not essential for rate zonal separation and other solutes (e.g., inorganic salts, polysaccharides, etc.) could also be employed. Approximately half of the initially loaded particles were recovered after fractionation; the rest were likely lost to precipitation or adsorption on the plastics/membranes during centrifugation and subsequent fractionation and purification.

Nanoparticle Synthesis. The details of the nanoparticle synthesis and characterization are found in ref 30. Briefly, the Fe_3O_4 cores were synthesized by thermal decomposition of iron(III) acetylacetonate at 300 °C, according to the method published by Xu et al. using oleylamine as capping agent.[31] Particle stabilization was obtained by ligand exchange with second generation dendritic PEG (M_w = 2477g·mol^{-1}) with a nitrocatechol anchoring group. Ligand exchange was performed in ethanol at 50 °C for 24 h with 4-fold weight excess of the stabilizer compared to the oleylamine-stabilized Fe_3O_4 NPs. After replacement of the ligands, the particles were separated out of solution by precipitation after adding hexane to the suspension and collected using a magnet; the oleylamine was then removed by decantation.

DOI: 10.1021/acs.langmuir.5b01811
Langmuir 2015, 31, 11179−11185

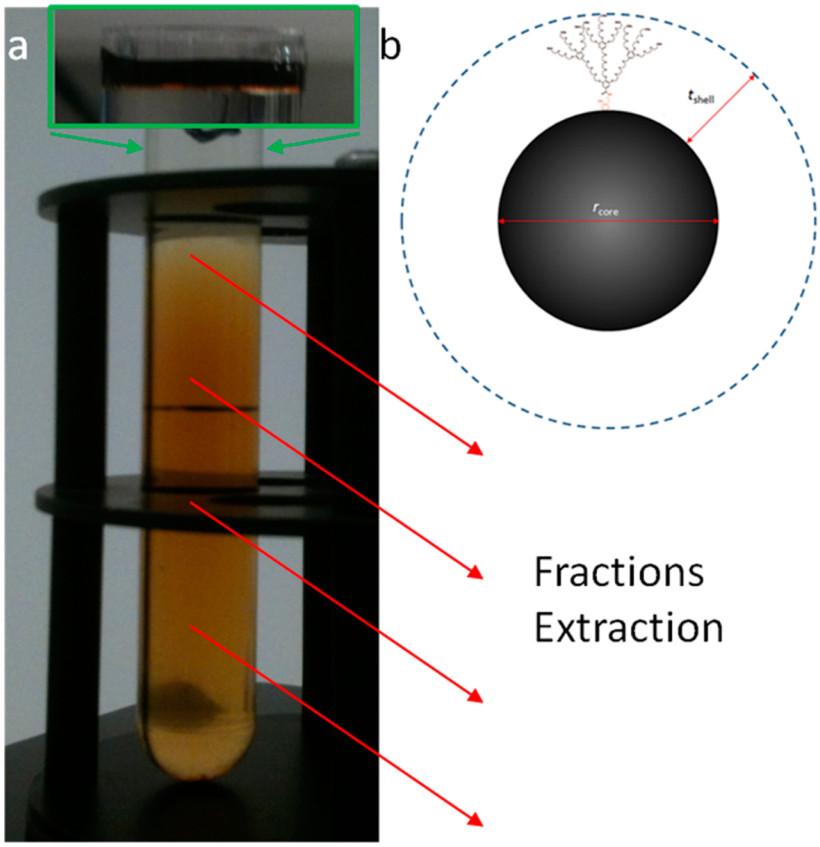

Figure 1. (a) NP sedimentation profile in the sucrose gradient after ultracentrifugation and schematic representation of the fractionation process. The inset shows the NP suspension loaded on top of the sucrose solution before centrifugation. (b) Schematic representation of the core−shell NPs.

After a second precipitation step, the particles were dried and resuspended in water, followed by centrifuge-assisted ultrafiltration.

TEM Image Analysis. Particle sizing from TEM images was carried out by an automated, custom-written algorithm using IDL (Exelis Visual Information Solutions, Inc.). The size distribution was extracted by binarizing the images using a threshold value to distinguish the particles from the background. The image-dependent threshold was chosen after plotting the intensity histogram of the images and identifying the peak corresponding to the particles. The correct choice of the threshold was confirmed by independently locating and counting the particles until the number of binarized regions corresponded to the particle number. The particle size distribution was then extracted from the area of each binarized region, assuming a circular cross section.

RESULTS AND DISCUSSION

For our experiments, we used iron oxide (Fe_3O_4) NPs whose surface is coated by a brush of second-generation dendritic PEG through nitrocatechol anchors. Details on the particle synthesis and characterization can be found in refs 30 and 32 (see the Experimental Section for more details). For the purpose of this paper, we report that the as-synthesized NPs have a core diameter of 8.4 ± 1.4 nm (from SAXS), a shell thickness of 4.3 nm from DLS and p of 0.10 (from DLS). The molecular weight of the second generation PEG dendrons is 2477 g·mol^{-1}, they have a grafting density of 0.73 ± 0.03 chains·nm^{-2} (from TGA) and the particles bear a slightly negative charge in 0.1 M HEPES buffer (pH = 7.4).

Nanoparticle fractionation was carried out according to the procedure described in ref 33. Briefly, a sucrose gradient was generated using the hybrid Gradient Station (BioComp Instruments, Inc.), capable of both gradient formation and piston fractionation. Aqueous nanoparticle solutions (10 mg·mL^{-1}) were carefully loaded onto 20−50 wt % sucrose gradients before 2 h of ultracentrifugation and subsequent fractionation (see the Experimental section for more detail). During centrifugation, NPs travel from the meniscus interface down along the gradient at a rate influenced greatly by their density (as described by Svedberg's equation). In particular, separation in rate zonal centrifugation depends critically on two parameters: particle density and particle size. For inorganic/organic core/shell NPs like the ones employed in this study, particle density rapidly increases with particle size, due to the growing influence of the dense metal core as the inorganic shell remains practically unchanged in thickness and density. The latter assumption is supported by previous analysis of the polymer grafting density on the surface of the NPs, showing that the grafting density, and thus the mass of polymer per particle, depends only on the molecular weight of the stabilizer and not on its architecture, that is, linear or dendritic.[30] Therefore, this excludes therefore the presence of strong curvature effects on the steric packing of the ligands on the surface of the particles, indicating that differently sized NPs have similar thickness and density of the stabilizing layer. This led to a broad and continuous profile of NPs along the tube that could be isolated by careful fractionation. Figure 1 shows the as-synthesized NPs suspension loaded on top of the sucrose solution and the sedimentation profile after ultracentrifugation. Seven NPs fractions were extracted from the gradient, the sucrose was thoroughly cleaned out and both the as-synthesized and the fractionated NPs were characterized by SAXS.

DOI: 10.1021/acs.langmuir.5b01811
Langmuir 2015, 31, 11179−11185

Before examining the NP fractions, we initially carried out calibration measurements on the as-synthesized suspensions in order to ascertain the concentration and form factor parameters related to the core−shell spherical NPs, that is, core radius, shell thickness, and polydispersity of the cores. Pristine freeze-dried spherical core−shell NPs were redispersed in water and the SAXS pattern was measured to confirm the validity of the fitting models used for this study and to fix given fitting parameters. In particular, we used a model based on the sum of the scattering intensity profiles coming from the form factor of a polydisperse spherical core−shell NPs model together with the scattering intensity profile coming from a power-law model. The second part crucially accounts for thermal fluctuations in the polymer layer to adjust the intensity of the scattering signal at low q-values.[34] The first part gives the form factor for polydisperse spherical NPs with a core−shell structure, with a polydisperse core and a constant shell thickness,[26] due to the monodispersity of the PEG dendrons (see the Experimental section for more details).

Figure 2 shows the scattering intensity profile for the as-synthesized dispersion of the spherical core−shell NPs. The

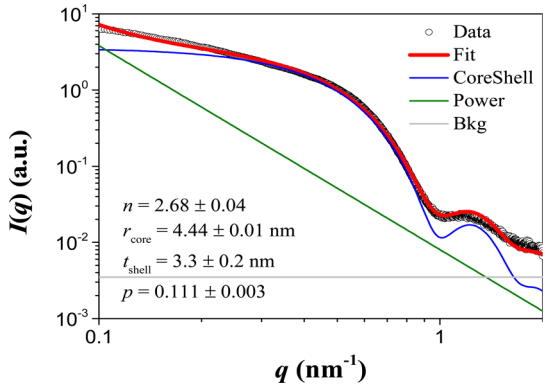

Figure 2. Scattering intensity profile (empty black symbols) and the form factor fitting curve (red). The polydisperse core−shell spherical particle model with a fixed shell thickness (t_{shell} = 3.3 ± 0.2 nm) is shown in blue and the power-law contribution coming from the fluctuations of the adsorbed polymer layer is shown in green. The gray line corresponds to the background.

results show the best agreement with a fitted core radius r_{core} = 4.44 ± 0.01 nm, a corresponding polydispersity value p = 0.111 ± 0.003 and a fixed shell thickness t_{shell} = 3.3 ± 0.2 nm. The scaling factor from the power-law model which yields the best fit is n = 2.68 ± 0.03, which differs from the 4/3 value predicted for linear polymers adsorbed onto the NPs surface. This difference might stem from the dendritic architecture of the stabilizing polymers, which cannot form blobs when swollen and present a higher rigidity. In particular, the fitted polymer thickness corresponds to ca. 80% of the fully stretched configuration predicted by Force Field Molecular Mechanics calculations (t_{MMFF94} = 4.1 nm). It is worth mentioning that, as shown in Figure 2, the use of a simple polydisperse spherical core−shell model was not able to capture the scattering intensity profile of our particles and that the power-law term was necessary for successful fitting at low q values.

We then constructed a calibration curve to be able to estimate the volume fraction of the NP suspensions by preparing and measuring suspensions of as-synthesized freeze-dried particles at different known concentrations (0.24, 0.11, 0.059, and 0.024 wt %, corresponding to 0.0458, 0.0211, 0.0114, and 0.00459 V/V-%) and plotting the measured scattered intensity at low q (q = 0.10 nm^{-1}) versus volume fraction (Supporting Information Figure SI-2). This also allowed us to exclude that, in this concentration range and below, any structure factor contribution was not present (Supporting Information Figure SI-1).

Next, we moved on to SAXS measurements of the NP fractions after ultracentrifugation. From the evaluation of the low q-value scattering intensities of all the fractions (Figure 3a), their concentration could be determined against the above-mentioned calibration (Figure 3b). In particular, this approach allowed to determine accurately volume fractions ranging between 5.5 × 10^{-6} and 4.6 × 10^{-4}, and the obtained volume fractions for the seven investigated fractions ranged from 5.9 × 10^{-6} to 5.2 × 10^{-5}. Due to the high contrast between the iron oxide core and the surrounding medium this technique is very sensitive to measure concentrations for such kind of NPs.

Finally, all scattering profiles from the collected fractions were fitted (Supporting Information Figure SI-3) to extract the particle radius and polydispersity of all the fractions. The fitted scattering data are reported in Figure 4, where the zoom in the inset highlights the region around the first minimum in $I(q)$. A shift in the minimum position toward the left indicates an increase in particle size.

First, we note that by collecting fractions at decreasing height along the sucrose gradient, the core radius continuously increases until reaching a plateau value at 4.69 ± 0.04 nm

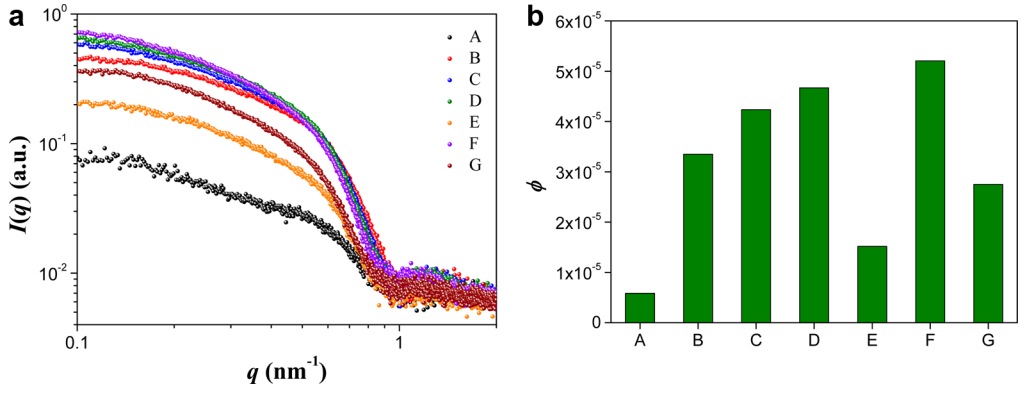

Figure 3. (a) Scattering intensity profiles for the seven collected fractions of the core−shell spherical nanoparticles (A to G). (b) NP concentration (volume fraction) for the seven fractions estimated from the calibration curve in Supporting Information Figure SI-2.

DOI: 10.1021/acs.langmuir.5b01811
Langmuir 2015, 31, 11179−11185

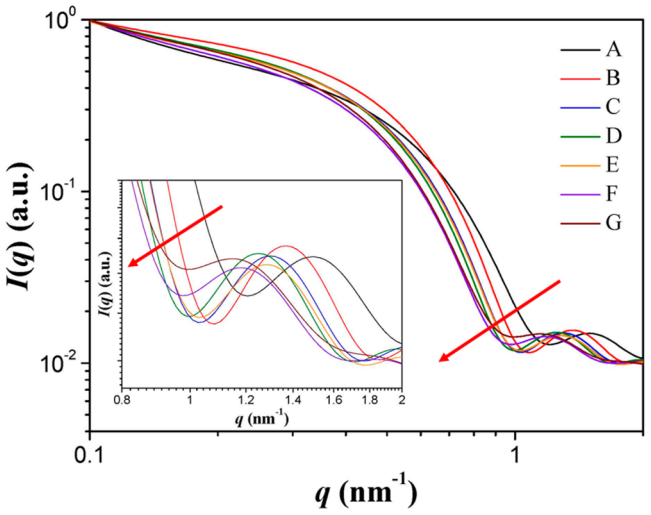

Figure 4. Fitted scattering intensity profiles for the seven fractions. Inset: zoom in the region of the first minimum of $I(q)$. The arrow indicates increasing average particle size.

(Figure 5a). The lower $r_{core}[A]$ = 3.8 ± 0.2 nm and the upper $r_{core}[G]$ = 4.67 ± 0.04 nm values for the NPs core radius fall quite nicely in the 2-sigma window obtained for the average value of the as synthesized dispersion ($r_{core}[O]-\sigma$ = 3.95 nm < r_{core} < $r_{core}[O] + \sigma$ = 4.93 nm, where O indicates the original, as synthesized suspension). We can already note that the size-distribution of each fraction is extremely narrow. More precise information on this can be obtained by evaluating the polydispersity index of the NPs fractions. Here, we observe that all fractions have a lower polydispersity than the as-synthesized particles (0.0001 < p < 0. 092, corresponding to percent standard deviations between 0.01% and 9.2%) always below to the one from the original nanoparticle dispersion p = 0.111 ± 0.003 (Figure 5b) and that the first three fractions exhibit extraordinarily low p values of the order of 10^{-4}. The sudden increase in p might be due to a deviation from linearity in the density gradient. In the future, this hypothesis can be tested by taking thinner slices out of the vial or by purposely imposing nonlinear density gradients.

Compared to standard size analysis from direct imaging, for example, by transmission electron microscopy, SAXS offers significantly higher accuracy and leads to more robust estimates of the average particle size and polydispersity. The main reason for this is mostly connected to the much higher statistics in scattering experiments, compared to the analysis of order 10^2–10^3 particles from TEM. Additionally, any particle sizing procedure using images entails a certain degree of arbitrariness in setting threshold parameters to separate the particles from the background (more details on the procedure we used are found in the Experimental section). To support these statements, we report the results of quantitative image analysis of the original suspension and of two fractions (E and G), as shown in the TEM images of Figure 6. For the as-synthesized sample, we obtained values of σ = 0.54 nm, r_{core} = 3.67 nm, and thus p = 0.15, measuring 5499 particles. For fraction E we got σ = 0.32 nm, r_{core} = 3.35 nm, and p = 0.10, analyzing 583 particles and for fraction G, σ = 0.43 nm, r_{core} = 3.53 nm, and p = 0.12, measuring 628 particles. In all cases, we see that image analysis overestimates polydispersity and underestimates the average particle size. The former is mainly due to statistics, whereas the latter is due to the choice of threshold intensity to maximize the number of measured particles without including any artifact form the background.

CONCLUSIONS

In conclusion, we have reinforced the finding that ultracentrifugation is a viable route to select highly monodisperse NP fractions out of as-synthesized, polydisperse suspensions. In particular, our results have shown that this route is viable not only for NPs stabilized by short molecular ligands, but that it is also successfully applicable to more complex core–shell objects with polymeric shells. Finally, we have also demonstrated that SAXS, as an ensemble method, is a rapid, robust, and sensitive tool to characterize the fractionation process with high accuracy.

The results of our work, therefore, are encouraging to extend this method to the separation of other complex nanoparticle systems to be able to work experimentally with truly monodisperse particles. In this way, a more direct comparison between numerical simulations (where polydispersity can be controlled at will) and experiments can be achieved and may pave the way for the realization of nanoparticle assemblies with fine control on the structure and thus of the material properties. Our findings are general and are not limited to the case of PEG-iron oxide nanoparticles, but can also be extended to other materials, for example, metallic nanoparticles stabilized by extended polymer shells. Monodispersity in the former case could be beneficial in relation to encapsulation within lipidic membranes,[35] whereas in the latter case, it may lead to the self-assembly of responsive nanoparticle arrays with well-defined optical properties.[36] The generality and robustness of our results open up the possibility to extend our isolation and

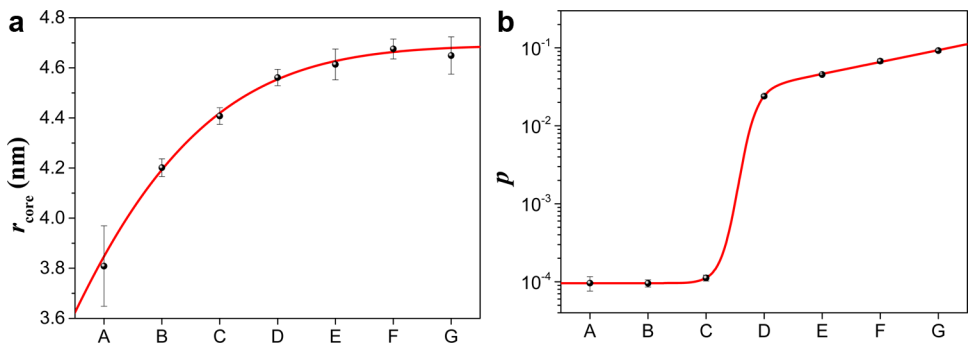

Figure 5. (a) Core radius and (b) polydispersity for the seven collected fractions of the core–shell spherical nanoparticles obtained from the form factor fitting curve of polydisperse spherical core–shell particles with a fixed shell thickness (t_{shell} = 3.3 ± 0.2 nm). Note: lines are guides to the eye.

DOI: 10.1021/acs.langmuir.5b01811
Langmuir 2015, 31, 11179–11185

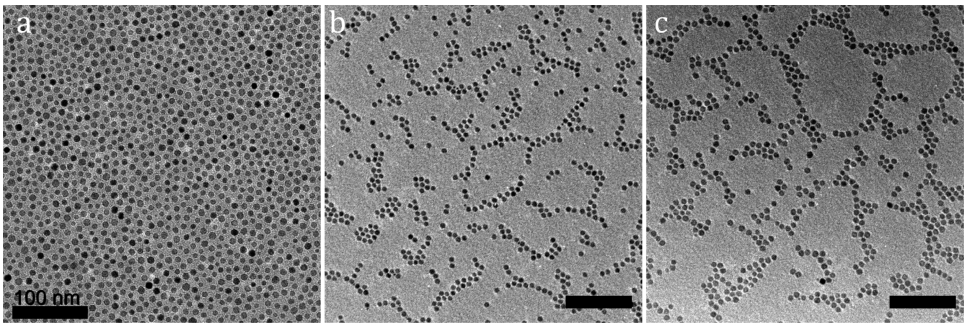

Figure 6. TEM images of the original suspension (a) and of fraction E (b) and G (c).

characterization procedure to even more complex core−shell objects, displaying shape or chemical anisotropy. Another interesting direction for future work may be to apply ultracentrifugation to separate nanoparticles with identical cores and stabilized by polymers of similar molecular weight but different architecture, for example, linear versus dendritic, to test the proficiency of the technique in decoupling particle mass from the details of the stabilizing polymer layer.

■ ASSOCIATED CONTENT

Supporting Information

The Supporting Information is available free of charge on the ACS Publications website at DOI: 10.1021/acs.langmuir.5b01811.

Additional details of the experimental procedures are found in the Supporting Information. (PDF)

■ AUTHOR INFORMATION

Corresponding Author

*E-mail: lucio.isa@mat.ethz.ch.

Notes

The authors declare no competing financial interest.

■ ACKNOWLEDGMENTS

The authors acknowledge Torben Gillich for the core−shell nanoparticle synthesis and Edmondo Benetti and Giulia Cargese for UV−vis spectroscopy analysis of the nanoparticles. L.I. acknowledges financial support from the Swiss National Science Foundation grant PP00P2_144646/1. F.S. and R.P.C. acknowledge support from the Swiss National Science Foundation.

■ REFERENCES

(1) Murray, C. B.; Kagan, C. R.; Bawendi, M. G. Synthesis and characterization of monodisperse nanocrystals and close-packed nanocrystal assemblies. *Annu. Rev. Mater. Sci.* **2000**, *30* (1), 545−610.

(2) Gasser, U. Crystallization in three- and two-dimensional colloidal suspensions. *J. Phys.: Condens. Matter* **2009**, *21* (20), 203101.

(3) Shevchenko, E. V.; Talapin, D. V.; Kotov, N. A.; O'Brien, S.; Murray, C. B. Structural diversity in binary nanoparticle superlattices. *Nature* **2006**, *439*, 55−59.

(4) Kravchyk, K.; Protesescu, L.; Bodnarchuk, M. I.; Krumeich, F.; Yarema, M.; Walter, M.; Guntlin, C.; Kovalenko, M. V. Monodisperse and Inorganically Capped Sn and Sn/SnO2 Nanocrystals for High-Performance Li-Ion Battery Anodes. *J. Am. Chem. Soc.* **2013**, *135* (11), 4199−4202.

(5) Kraus, T.; Malaquin, L.; Schmid, H.; Riess, W.; Spencer, N. D.; Wolf, H. Nanoparticle printing with single-particle resolution. *Nat. Nanotechnol.* **2007**, *2* (9), 570−576.

(6) Anker, J. N.; Hall, W. P.; Lyandres, O.; Shah, N. C.; Zhao, J.; Van Duyne, R. P. Biosensing with plasmonic nanosensors. *Nat. Mater.* **2008**, *7* (6), 442−453.

(7) Van Lehn, R. C.; Atukorale, P. U.; Carney, R. P.; Yang, Y.-S.; Stellacci, F.; Irvine, D. J.; Alexander-Katz, A. Effect of Particle Diameter and Surface Composition on the Spontaneous Fusion of Monolayer-Protected Gold Nanoparticles with Lipid Bilayers. *Nano Lett.* **2013**, *13* (9), 4060−4067.

(8) Bastús, N. G.; Comenge, J.; Puntes, V. Kinetically Controlled Seeded Growth Synthesis of Citrate-Stabilized Gold Nanoparticles of up to 200 nm: Size Focusing versus Ostwald Ripening. *Langmuir* **2011**, *27* (17), 11098−11105.

(9) Stöber, W.; Fink, A.; Bohn, E. Controlled growth of monodisperse silica spheres in the micron size range. *J. Colloid Interface Sci.* **1968**, *26* (1), 62−69.

(10) Surugau, N.; Urban, P. L. Electrophoretic methods for separation of nanoparticles. *J. Sep. Sci.* **2009**, *32* (11), 1889−1906.

(11) Sajeesh, P.; Sen, A. Particle separation and sorting in microfluidic devices: a review. *Microfluid. Nanofluid.* **2014**, *17* (1), 1−52.

(12) Svedberg, T.; Rinde, H. The ultra-centrifuge, a new instrument for the determination of size and distribution of size of particle in amicroscopic colloids. *J. Am. Chem. Soc.* **1924**, *46* (12), 2677−2693.

(13) Planken, K. L.; Colfen, H. Analytical ultracentrifugation of colloids. *Nanoscale* **2010**, *2* (10), 1849−1869.

(14) Miller, J. B.; Harris, J. M.; Hobbie, E. K. Purifying Colloidal Nanoparticles through Ultracentrifugation with Implications for Interfaces and Materials. *Langmuir* **2014**, *30* (27), 7936−7946.

(15) Manoharan, V. N.; Elsesser, M. T.; Pine, D. J. Dense packing and symmetry in small clusters of microspheres. *Science* **2003**, *301* (5632), 483−487.

(16) Wang, Y.; Wang, Y.; Breed, D. R.; Manoharan, V. N.; Feng, L.; Hollingsworth, A. D.; Weck, M.; Pine, D. J. Colloids with valence and specific directional bonding. *Nature* **2012**, *491* (7422), 51−55.

(17) Mastronardi, M. L.; Hennrich, F.; Henderson, E. J.; Maier-Flaig, F.; Blum, C.; Reichenbach, J.; Lemmer, U.; Kübel, C.; Wang, D.; Kappes, M. M.; Ozin, G. A. Preparation of Monodisperse Silicon Nanocrystals Using Density Gradient Ultracentrifugation. *J. Am. Chem. Soc.* **2011**, *133* (31), 11928−11931.

(18) Miller, J. B.; Van Sickle, A. R.; Anthony, R. J.; Kroll, D. M.; Kortshagen, U. R.; Hobbie, E. K. Ensemble Brightening and Enhanced Quantum Yield in Size-Purified Silicon Nanocrystals. *ACS Nano* **2012**, *6* (8), 7389−7396.

(19) Bai, L.; Ma, X.; Liu, J.; Sun, X.; Zhao, D.; Evans, D. G. Rapid Separation and Purification of Nanoparticles in Organic Density Gradients. *J. Am. Chem. Soc.* **2010**, *132* (7), 2333−2337.

(20) Carney, R. P.; Kim, J. Y.; Qian, H. F.; Jin, R. C.; Mehenni, H.; Stellacci, F.; Bakr, O. M. Determination of nanoparticle size distribution together with density or molecular weight by 2D analytical ultracentrifugation. *Nat. Commun.* **2011**, *2*, 335.

(21) Sun, X.; Luo, D.; Liu, J.; Evans, D. G. Monodisperse Chemically Modified Graphene Obtained by Density Gradient Ultracentrifugal Rate Separation. *ACS Nano* **2010**, *4* (6), 3381−3389.

DOI: 10.1021/acs.langmuir.5b01811
Langmuir 2015, 31, 11179−11185

(22) Fagan, J. A.; Becker, M. L.; Chun, J.; Nie, P.; Bauer, B. J.; Simpson, J. R.; Hight-Walker, A.; Hobbie, E. K. Centrifugal Length Separation of Carbon Nanotubes. *Langmuir* **2008**, *24* (24), 13880−13889.
(23) Arnold, M. S.; Stupp, S. I.; Hersam, M. C. Enrichment of Single-Walled Carbon Nanotubes by Diameter in Density Gradients. *Nano Lett.* **2005**, *5* (4), 713−718.
(24) Pedersen, J. S. Analysis of small-angle scattering data from colloids and polymer solutions: modeling and least-squares fitting. *Adv. Colloid Interface Sci.* **1997**, *70*, 171−210.
(25) Kline, S. Reduction and analysis of SANS and USANS data using IGOR Pro. *J. Appl. Crystallogr.* **2006**, *39* (6), 895−900.
(26) Bartlett, P.; Ottewill, R. H. A neutron scattering study of the structure of a bimodal colloidal crystal. *J. Chem. Phys.* **1992**, *96* (4), 3306−3318.
(27) Guinier, A.; Fournet, G. *Small-Angle Scattering of X-Rays*; John Wiley and Sons: New York, 1955.
(28) Hayter, J. *Physics of Amphiphiles, Micelles, Vesicles and Microemulsions*; Degiorgio, V., Corti, M., Eds.; North-Holland: Amsterdam, 1983.
(29) Kotlarchyk, M.; Chen, S. H. Analysis of small angle neutron scattering spectra from polydisperse interacting colloids. *J. Chem. Phys.* **1983**, *79* (5), 2461−2469.
(30) Gillich, T.; Acikgöz, C.; Isa, L.; Schlüter, A. D.; Spencer, N. D.; Textor, M. PEG-Stabilized Core−Shell Nanoparticles: Impact of Linear versus Dendritic Polymer Shell Architecture on Colloidal Properties and the Reversibility of Temperature-Induced Aggregation. *ACS Nano* **2013**, *7* (1), 316−329.
(31) Xu, Z.; Shen, C.; Hou, Y.; Gao, H.; Sun, S. Oleylamine as Both Reducing Agent and Stabilizer in a Facile Synthesis of Magnetite Nanoparticles. *Chem. Mater.* **2009**, *21* (9), 1778−1780.
(32) Isa, L.; Calzolari, D. C. E.; Pontoni, D.; Gillich, T.; Nelson, A.; Zirbs, R.; Sanchez-Ferrer, A.; Mezzenga, R.; Reimhult, E. Core-shell nanoparticle monolayers at planar liquid-liquid interfaces: effects of polymer architecture on the interface microstructure. *Soft Matter* **2013**, *9* (14), 3789−3797.
(33) Carney, R. P.; Astier, Y.; Carney, T. M.; Voïtchovsky, K.; Jacob Silva, P. H.; Stellacci, F. Electrical Method to Quantify Nanoparticle Interaction with Lipid Bilayers. *ACS Nano* **2013**, *7* (2), 932−942.
(34) Auvray, L.; Gennes, P. G. d. Neutron Scattering by Adsorbed Polymer Layers. *EPL (Europhysics Letters)* **1986**, *2* (8), 647.
(35) Amstad, E.; Kohlbrecher, J.; Müller, E.; Schweizer, T.; Textor, M.; Reimhult, E. Triggered Release from Liposomes through Magnetic Actuation of Iron Oxide Nanoparticle Containing Membranes. *Nano Lett.* **2011**, *11* (4), 1664−1670.
(36) Vogel, N.; Fernández-López, C.; Pérez-Juste, J.; Liz-Marzán, L. M.; Landfester, K.; Weiss, C. K. Ordered Arrays of Gold Nanostructures from Interfacially Assembled Au@PNIPAM Hybrid Nanoparticles. *Langmuir* **2012**, *28* (24), 8985−8993.

DOI: 10.1021/acs.langmuir.5b01811
Langmuir 2015, 31, 11179−11185